PNAS RESEARCH ARTICLE | BIOPHYSICS AND COMPUTATIONAL BIOLOGY

A unified model for the dynamics of ATP-independent ultrafast contraction

Carlos Floyd[a], Arthur T. Molines[b], Xiangting Lei[c], Jerry E. Honts[d], Fred Chang[b], Mary Williard Elting[e,1], Suriyanarayanan Vaikuntanathan[a,1], Aaron R. Dinner[a,1], and M. Saad Bhamla[c,1]

Edited by Herbert Levine, Northeastern University, Boston, MA; received October 17, 2022; accepted May 1, 2023

In nature, several ciliated protists possess the remarkable ability to execute ultrafast motions using protein assemblies called myonemes, which contract in response to Ca^{2+} ions. Existing theories, such as actomyosin contractility and macroscopic biomechanical latches, do not adequately describe these systems, necessitating development of models to understand their mechanisms. In this study, we image and quantitatively analyze the contractile kinematics observed in two ciliated protists (*Vorticella* sp. and *Spirostomum* sp.), and, based on the mechanochemistry of these organisms, we propose a minimal mathematical model that reproduces our observations as well as those published previously. Analyzing the model reveals three distinct dynamic regimes, differentiated by the rate of chemical driving and the importance of inertia. We characterize their unique scaling behaviors and kinematic signatures. Besides providing insights into Ca^{2+}-powered myoneme contraction in protists, our work may also inform the rational design of ultrafast bioengineered systems such as active synthetic cells.

ultrafast motion | calcium-powered dynamics | protist physiology | mechanochemical modeling | synthetic biology

Significance

The myoneme-based contractile apparatus, responsible for the ultrafast motions of certain protozoa, presents an excellent opportunity for engineering control over subcellular biomechanics. However, its basic dynamical properties remain poorly understood. Unlike actomyosin contraction, which is ATP-driven and has been extensively modeled, myoneme-based contraction is Ca^{2+}-driven and lacks a comprehensive mechanochemical description that covers its manifestations in various organisms. In this study, we derive a minimal continuum model that semiquantitatively explains experimental measurements and use it to uncover distinct operating regimes of myoneme-based contraction. We demonstrate that the dynamics rely on three timescales representing chemical driving, material stiffness, and viscous drag. These findings carry broad implications for mechanochemical force generation, protozoan evolution, and synthetic biology.

A well-known molecular mechanism for motion in biological systems is actomyosin contractility, which involves the relative sliding of actin filaments due to ATP hydrolysis by bound molecular motors (1). However, the fastest motions currently known to occur in the biological world (measured as the proportional change in length per unit time) are due not to actomyosin assemblies but to lesser-known protein assemblies called myonemes (2–4). We use "myonemes" in the broadest sense (5), encompassing terms used for specific organisms such as "spasmonemes" and "M-bands." Myonemes are common in ciliated protists: For example, they are found in the wine glass-shaped genus *Vorticella* (6, 7), the cigar-shaped genus *Spirostomum* (8–11), the trumpet-shaped genus *Stentor* (12, 13), the tear drop-shaped genus *Lacrymaria* (14), and the chandelier-shaped genus *Zoothamnium* (15, 16). Similar Ca^{2+}-responsive supramolecular assemblies are proposed to occur in a range of other single-celled organisms (17–24), and possibly even plants (25–27). The mechanism of ultrafast myoneme contraction is qualitatively different from actomyosin contraction in that ATP is not directly consumed during the contractile motion (6, 28). Instead, a local increase in Ca^{2+} concentration acts as a mechanical actuator to initiate contraction (29–32). ATP is subsequently consumed to pump Ca^{2+} away from the myoneme fibers and reset the process (15, 33).

While several experimental studies have been conducted on myoneme-based contraction dynamics (7–10, 15, 34–42), it is difficult to draw general conclusions without a theoretical framework to interpret the observations. Whereas actomyosin contractility has been extensively studied theoretically and computationally (43–48), Ca^{2+}-powered myoneme-based contractility is relatively unexplored from a modeling point of view. An existing computational model of *Vorticella* (49) is specific to the geometry of the organism and thus does not apply across species. Previous mechanochemical analyses also do not address the dynamics of contraction (6, 9). Questions that a mathematical model of myoneme contraction might address are: What synchronizes contraction across the organism's length, what sets the rate of chemical driving, and what are the key geometric and mechanical factors that affect the contraction dynamics?

Here, we develop a minimal mathematical model of myoneme contraction and show that it applies across species (Fig. 1). In our model, an elastic medium in a dissipative environment is driven out of equilibrium by a traveling wave of shrinking rest lengths, which captures the effect of a traveling Ca^{2+} wave. This simple setup omits several system-specific details but can fit experimental contraction measurements for *Spirostomum* and *Vorticella*. Mathematically, the model comprises a wave equation

This article is a PNAS Direct Submission.

[1]To whom correspondence may be addressed. Email: mary.elting@ncsu.edu, svaikunt@uchicago.edu, dinner@uchicago.edu, or saadb@chbe.gatech.edu.

This article contains supporting information online at https://www.pnas.org/lookup/suppl/doi:10.1073/pnas.2217737120/-/DCSupplemental.

Published June 12, 2023.

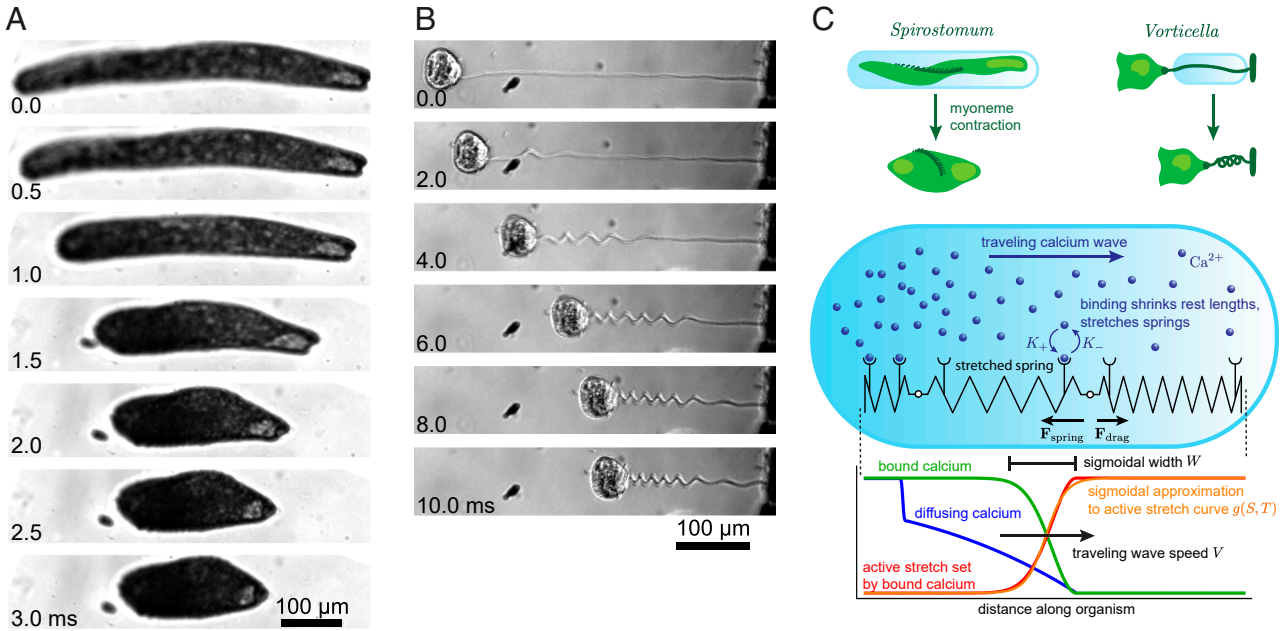

Fig. 1. Myoneme-based contraction in ciliated protists. (*A*) Images of *Spirostomum* undergoing contraction, with the time in milliseconds labeled on the bottom left of each image. Rapid contraction begins at $T = 0$ ms and is followed by a slower reelongation phase (not depicted). Note that the left side of the organism begins contracting (between 0.5 and 1.0 ms) before the right (between 1.0 and 1.5 ms). (*B*) Same as (*A*) for *Vorticella*. (*C*) Schematic of the model. The contractile body of *Spirostomum* and stalk of *Vorticella* are abstracted as a 1D elastic medium in a viscous environment, represented as a chain of springs. The local spring rest length (depicted as the number of ridges) depends on the number of bound Ca^{2+} ions (shown as blue spheres bound to receptors on the springs). A rightward traveling Ca^{2+} wave thus shrinks the spring rest lengths, exerting forces in the chain which then contracts against viscous drag. The bottom graph schematically illustrates several quantities in our mechanochemical model at a fixed time, which we elaborate on in the main text.

with dissipation and a nonautonomous source term. We derive an approximate form for the nonautonomous function by analyzing an auxiliary kinetic model for a traveling Ca^{2+} wave. Using the model, we show that the balance between chemical driving, mechanical stiffness, and viscous drag results in three dynamic regimes. These regimes are distinguished by the relative importance of inertia and Ca^{2+} wave speed, and they exhibit kinematic signatures, including asymmetric contraction and different scaling behavior of the maximum contraction rate. This work provides a starting point for extracting general mechanochemical principles of myoneme contraction in biological and engineered systems.

1. Model Derivation

Myoneme contraction is driven by an increase in cytosolic Ca^{2+}, which occurs as a traveling wave that traverses the organism's length in several milliseconds (30, 49–52). The mechanism by which Ca^{2+} physically induces contraction is believed to be a screened entropic spring effect: Ca^{2+} binds to the negatively charged myoneme fibers and screens their electrostatic self-repulsion, which allows for the entropic contribution to the free energy to induce collapse of the polymer (53). This system is sometimes considered a polyelectrolyte gel, in which thermodynamic balances of entropic and osmotic forces determine the gel's equilibrium (15, 54, 55). The precise contributions to the myoneme free energy as a function of length are not needed to formulate a minimal mechanical model, and we make the phenomenological assumption that the system obeys linear elasticity (56). The key difference from the usual elastic theory is that the rest lengths of the elastic elements are dynamic quantities that depend on the local concentration of bound Ca^{2+} (Fig. 1*C*).

To formulate the model mathematically, we start from a discrete chain of harmonic springs in one dimension with externally imposed rest lengths, and we define $X_i(T)$ as the position of the i^{th} mass at time T. The spring stiffness parameter k, mass m, drag γ, and initial rest length δ, are the same for all springs, and the instantaneous rest length $G_{i+\frac{1}{2}}(T)$ of the spring connecting masses i and $i+1$ is a nonautonomous function which we specify later. The force on mass i is

$$m\partial_T^2 X_i = k\left(X_{i+1} - X_i - G_{i+\frac{1}{2}}\right) - k\left(X_i - X_{i-1} - G_{i-\frac{1}{2}}\right) - \gamma\,\partial_T X_i. \quad [1]$$

Rather than a discrete description in terms of the index i, we seek a continuum description of the dynamics in terms of a material coordinate $S \in [0, L]$, where L is the uncontracted length of the system. By Taylor expanding the functions X and $g \equiv G/\delta$ to second order in δ and then letting $\delta \to 0$, we find the following partial differential equation (PDE) for the position $X(S, T)$:

$$\partial_T^2 X - \alpha\left(\partial_S^2 X - \partial_S g\right) + \mu\partial_T X = 0. \quad [2]$$

Here, $\alpha = k\delta^2/m = E_{\text{M}}A/\widetilde{m}$ is the product of Young's modulus E_{M} and the effective spring cross-sectional area A divided by the linear mass density $\widetilde{m} = m/\delta$ [where we used $k = E_{\text{M}}A/\delta$ (56)]. The parameter α can be interpreted as the square of the speed of sound in the spring chain (57). $\mu = \gamma/\delta\widetilde{m}$ is the ratio of the drag constant per unit length to the linear mass density, and $g(S, T)$ is a nonautonomous function for the active stretch, defined as the ratio of the current spring rest length $G(S, T)$ to the initial rest length δ. The quantities g, α, and μ remain finite as $\delta \to 0$ because $G \sim \delta$, $k \sim \delta^{-1}$, $m \sim \delta$ and $\gamma \sim \delta$, while E_{M}, A, and $\widetilde{m}$ are independent of δ. Eq. **2**

represents the force balance of $X(S, T)$, where the first term is the acceleration, the second term (proportional to α) captures the force due to the difference between the local stretch and the active stretch g, and the third term captures the drag force. See *SI Appendix, Supplementary Methods, section A* for a detailed derivation of the model.

We find the boundary conditions by retaking the continuum limit at the terminal masses in the discrete representation (Eq. **1**), noting that these masses are connected to only a single spring. This yields the stress-free condition

$$\partial_S X(S, T) = g(S, T) \text{ at } S = 0,\ L. \quad [3]$$

In the case of *Vorticella*, which has one end (say $S = L$) attached to a fixed substrate, we use the boundary condition $X(L, T) = L$ at that end. We further take the initial conditions

$$X(S, 0) = S \text{ and } \partial_T X(S, 0) = 0. \quad [4]$$

We model the active stretch $g(S, T)$ as a linear function of the local concentration of Ca^{2+} bound to the myoneme fibers; see Eq. **17**. Specifying the active stretch function $g(S, T)$ requires describing the Ca^{2+} dynamics, for which we adapt a tractable reaction–diffusion model of a traveling Ca^{2+} wave (58), as described in *Materials and Methods*, Ca^{2+} dynamics and *SI Appendix, Supplementary Methods, section B*. By analyzing this model, we find that a good approximation to the active stretch function $g(S, T) = g^*(S - VT; W)$ is a traveling wave moving at speed V and having a sigmoidal profile g^* with width W (Eq. **22**; Fig. 1*C*). This function decreases from 1 to $g_{\min} \in [0, 1]$ as the wave passes through the organism. An additional parameter O sets the time offset such that the center of the wave arrives at $S = 0$ at time O. As described in *Results*, section B, we can approximately express V and W in terms of the kinetic parameters of the Ca^{2+} model (Eqs. **5** and **6**).

Our model neglects contributions from transverse dimensions and twisting effects, which may alter the one-dimensional dynamics through elastic coupling in the real system (59, 60). As explained in *SI Appendix, Supplementary Methods, section C*, we assume that this coupling is negligible as a first approximation. In that section, we also discuss the explicit assumptions needed to disregard the poroelastic contribution arising from fluid motion around the organelles inside the contracting organism. We demonstrate that under standard approximations made when treating cytoplasm poroelasticity (61), poroelasticity in our model contributes an additive term to the Stokes drag coefficient (*SI Appendix, Supplementary Methods*, Eq. **50**). Moreover, we examine a model extension in which motion encounters resistance from auxiliary elastic elements with unchanged rest lengths during Ca^{2+} binding. This representation approximates, for instance, the microtubule sheath under the cortex of *Spirostomum* (11, 36) or the elastic stalk supporting the thin myoneme fiber in *Vorticella* (49). We show that a linear change of variables effectively maps the model with auxiliary elastic elements to the model presented here.

2. Results

A. A Minimal Continuum Model Reproduces Contraction Kinematics. Despite the model's simplicity, we find that it reproduces the contraction kinematics of *Spirostomum* and *Vorticella* semiquantitatively. We illustrate this by comparing the trajectories of normalized length $\lambda(T) \equiv (X(L, T) - X(0, T))/L$ from experimental measurements to fitted model curves. Contraction events for *Spirostomum* and *Vorticella* are shown in *SI Appendix*, Movies S1 and S2, and the experimental methods are described in *Materials and Methods*, Experimental methods. The second-order nonautonomous PDE model does not have an exact closed-form solution, though we describe exact series solutions in two limiting cases in *Results*, section C. To fit the model, we numerically integrate the PDE with different choices of parameters and compare the results to the experimental traces. See *Materials and Methods*, Computational methods for details on the computational methods. In Fig. 2*A*, we show five contraction measurements in *Spirostomum* along with a model solution fitted to their average, illustrating the feasibility of our model in capturing the contraction dynamics. The corresponding contraction velocities $|\partial_T \lambda|$ are shown in Fig. 2*B*. We also fit the model with a fixed boundary condition at $S = L$ to data for five *Vorticella* contraction events (Fig. 2 *C* and *D*).

In *SI Appendix*, Figs. S6 and S7, we present fits for each of the ten individual trajectories shown in Fig. 2 *A* and *C*, demonstrating that we can obtain excellent fits for all trajectories using fairly consistent parameters for each organism. As we explain in *Results*, section C, we find that these contraction events occur in a regime where inertia is unimportant, meaning that the dynamics are approximately determined only by the ratio μ/α. We fit the simplified "slow-wave" model (cf. Eq. **10**) and obtain a typical set of parameters for *Spirostomum*: $L = 0.58$ mm, $g_{\min} = 0.35$, $\mu/\alpha = 5$ ms/mm^2, $V = 0.8$ mm/ms, and $W = 0.18$ mm. For *Vorticella*, a typical set of parameters is $L = 0.27$ mm, $g_{\min} = 0.32$, $\mu/\alpha = 1$ ms/mm^2, $V = 0.23$ mm/ms, and $W = 0.08$ mm. In *SI Appendix, Supplementary Results, section B*, we demonstrate that the fitted parameters for *Vorticella* are consistent in order of magnitude with physiological parameters used in a detailed computational model in ref. 49. According to a two-tailed t test, the distributions of quantities μ/α, V, and W each have means that are statistically different for the two organisms (t test P-value $\ll 0.05$). In the following section, we investigate the kinetic factors that underlie the rate of chemical driving captured by the parameters V and W.

B. Ca^{2+} Dynamics Control Contraction. The speed V and, less intuitively, the width W of the active stretch wave $g(S - VT; W)$ determine how rapidly the length changes over time. As W decreases, the active stretch wave approaches a traveling step function in which the springs ahead of the wave have their original rest lengths, and those behind have rest lengths which are reduced by a factor $g_{\min}$. As W increases, the distribution of changing rest lengths widens, and the driving and relaxation become more spatially and temporally homogeneous. We illustrate this in Fig. 2*E*, where we show the length trajectory for several values of W.

We are interested in understanding which features of the Ca^{2+} dynamics control the quantities V and W, since these parameters control the rate at which the mechanical system is chemically driven out of equilibrium. To do this, we analyzed a kinetic model (58) for a traveling Ca^{2+} wave powered by calcium-induced calcium release (62, 63) from an out-of-equilibrium internal store [e.g., the endoplasmic reticulum (30, 50)] into the cytosol. It has been previously shown that in this model, the wave speed V approximately follows (58)

$$V \approx \sqrt{\frac{JD_C}{C_0}}, \quad [5]$$

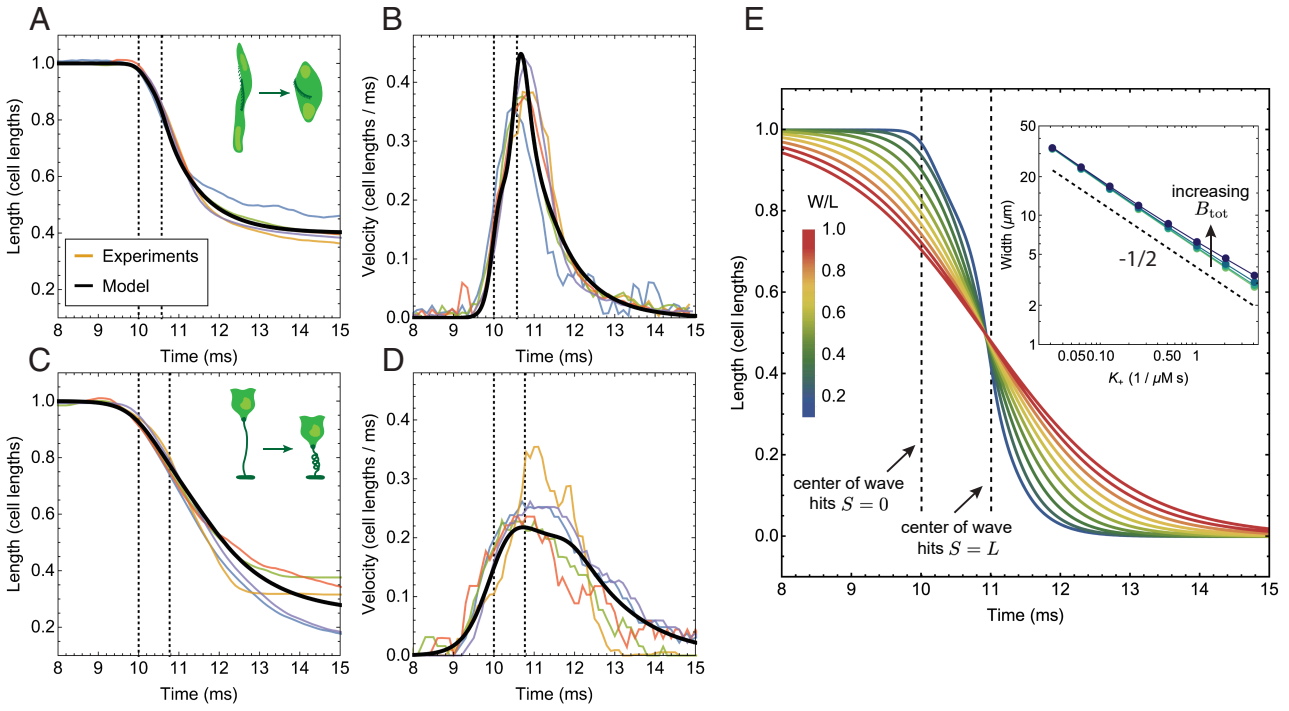

Fig. 2. Comparison of the model to experimental data. (*A*) Five measurements of *Spirostomum* contraction, collapsed to the same scale by normalizing length using the organism's uncontracted length L and by offsetting time so that contraction begins around $T = 10$ ms. Thin lines represent individual contraction events, and we color each differently. The thick black curve shows the model fit to all of these trajectories at once; see *SI Appendix, Supplementary Results, section B* for fits to the individual curves. Vertical dashed lines indicate the times in the model solution when the center of the active stretch wave arrives at $S = 0$ and $S = L$. Time is shifted by choosing $O = 10$ ms in Eq. **22** to achieve numerical agreement between the boundary and initial conditions (see *Material and Methods*, Computational methods). (*B*) The corresponding rate trajectories, obtained by numerically differentiating the data in (*A*). Colors of individual events are the same as in (*A*). (*C* and *D*) The same as (*A*) and (*B*) but for *Vorticella* contraction. (*E*) Simulated length trajectories with $V = 1$ L/ms, $\alpha = 2$ $(L/\text{ms})^2$, $g_{\min} = 0$, $O = 10$ ms, and $\mu = 10$ ms^{-1}. The width W of the wave is varied from 0.1 L to 1.0 L in steps of 0.1 L as the colors range from blue to red. The inset shows how W depends on the binding rate K_+ in the Ca^{2+} model. The total myoneme concentration B_{tot} ranges from 500 to 4, 000 μM in multiples of 2 as the colors range from light green to purple. The dashed line in the inset represents the analytically predicted scaling $W \sim K_+^{-1/2}$. For the remaining parameters used in the *Inset*, see *SI Appendix*, Table S4.

where J represents the Ca^{2+} influx of open channels, D_C is the diffusion constant of Ca^{2+}, and C_0 is the concentration threshold of the Ca^{2+} channels (see *Materials and Methods*, Ca^{2+} dynamics and *SI Appendix, Supplementary Methods, section B* for more details). We incorporated the binding of cytosolic Ca^{2+} to myoneme fibers into the model and derived a relationship for the width W of the resulting active stretch wave:

$$W \approx \sqrt{\frac{D_C}{K_+ C_0}}, \qquad [6]$$

where K_+ is the rate at which Ca^{2+} binds to myonemes. We provide numerical confirmation of this relationship in *SI Appendix, Supplementary Methods, section B* and the *Inset* of Fig. 2*E*. A seemingly restrictive assumption made in the derivation of Eq. **6** is that the total concentration of myoneme binding sites B_{tot} is much smaller than the typical cytosolic Ca^{2+} concentration. However, we find numerically that the predicted scaling holds even as B_{tot} increases to relatively large values.

This analysis reveals that features in the dynamics of contraction, such as the time taken for the length to change, can inform us about the magnitudes of the underlying biophysical parameters like the binding rate K_+. Assuming D_C remains the same in both organisms [though the presence of internal buffers could affect this (58)], the estimated values of V and W for *Vorticella* and *Spirostomum* suggest, through Eqs. **5** and **6**, that these organisms possess different threshold Ca^{2+} concentrations C_0 (30, 64, 65) and different release rates J or binding constants K_+. This minimal model serves as a first step in connecting contraction dynamics to the organisms' biochemistry, but more in vivo experiments are necessary to test these predictions.

C. Dimensional Analysis Reveals the Minimal Set of Model Parameters. The model considered so far (Eq. **2** together with Eq. **22**) is written in dimensional quantities and depends on the parameters α and μ, which are related to the stiffness of the material and viscosity of the environment, and V, W, and $g_{\min}$, which are the speed, width, and minimum value of the active stretch wave. However, these parameters are not all independent. We now reduce the number of parameters by one through nondimensionalization. We use lowercase variables throughout to denote dimensionless quantities.

There are two length scales, W and L, and we pick the uncontracted length L as the reference length and define $s = S/L$, $x = X/L$, and $w = W/L$. Next, three timescales can be defined:

$$\tau_w = \frac{L}{V}, \ \tau_m = \frac{L}{\sqrt{\alpha}}, \text{ and } \tau_d = \frac{1}{\mu}. \qquad [7]$$

Here, τ_w is the wave timescale, which represents the time taken for the center of the traveling wave to traverse the length L; τ_m is the material timescale, which represents the time taken for a sound wave to traverse the length of the spring chain; τ_d is

the drag timescale, characterizing the exponential deceleration of motion due to viscous damping. Unless otherwise specified, we nondimensionalize time using $t = T/\tau_w$. In these units, the wave speed is equal to 1, and Eq. **2** is expressed as the following PDE for $x(s, t)$:

$$\partial_t^2 x - \eta_{w,m}^2 \left(\partial_s^2 x - \partial_s f^*(s-t)\right) + \eta_{w,d}\partial_t x = 0, \qquad [8]$$

where $f^*(s) \equiv g^*(Ls)$ is the active stretch wave profile, rewritten to take a dimensionless argument s. The size of τ_w relative to the two remaining timescales defines the nondimensional parameters

$$\eta_{w,m} \equiv \frac{\tau_w}{\tau_m} = \frac{\sqrt{\alpha}}{V} \text{ and } \eta_{w,d} \equiv \frac{\tau_w}{\tau_d} = \frac{\mu L}{V}. \qquad [9]$$

The parameter $\eta_{w,m}$ describes the ratio of the myonemal speed of sound (which depends on the stiffness and density) to the wave traversal speed, and it is independent of length. The parameter $\eta_{w,d}$ describes the ratio of the drag timescale (depending on viscosity and density) to the wave traversal speed and is proportional to the length.

We can further simplify these nondimensional dynamics by taking the "slow wave" limit $\eta_{w,m},\ \eta_{w,d} \gg 1$, in which Eq. **8** reduces to

$$\partial_t x - \zeta\left(\partial_s^2 x - \partial_s f^*(s-t)\right) = 0, \qquad [10]$$

where the only remaining parameter is

$$\zeta \equiv \frac{\tau_d \tau_w}{\tau_m^2} = \frac{\alpha}{V\mu L}. \qquad [11]$$

Eq. **10** can be viewed as an overdamped limit of the model, in which inertia has dropped out of the dynamics because only a first derivative with respect to time remains, and in which mass is no longer relevant because ζ is independent of $\widetilde{m}$.

Eq. **10** is similar to the diffusion (or heat) equation with a source term. One difference is the boundary conditions: typically, the heat equation has fixed Dirichlet or Neumann boundary conditions, yet x obeys a boundary condition that depends in time on $f^*(s-t)$ (cf. Eq. **3**). However, we can define

$$h(s, t) = \partial_s x(s, t) - f^*(s-t), \qquad [12]$$

and express Eq. **10** as

$$\partial_t h - \zeta\partial_s^2 h = -\partial_t f^*(s-t). \qquad [13]$$

The boundary conditions are now the fixed Dirichlet conditions $h(0, t) = h(1, t) = 0$, and thus Eq. **13** is exactly the diffusion equation with a source term $-\partial_t f$, for which exact series solutions can be found. The mixed boundary conditions of *Vorticella* also result in mixed boundary conditions for the diffusion equation.

We also consider a "quench" limit $\eta_{w,d},\ \eta_{w,m} \ll 1$, in which the traveling wave moves at infinite speed, such that the rest lengths of all the springs are set to their new values before the organism can react. This implies that $f(s)$ is independent of time. Because the timescale τ_w is zero if the wave is infinitely fast, we instead nondimensionalize time using τ_m in the quench limit. The dynamics consist of only the relaxation of the system to its equilibrium

$$x^{\text{eq}}(s) = \int_0^s f(s')ds'. \qquad [14]$$

The deviation from equilibrium, $y(s, t) \equiv x(s, t) - x^{\text{eq}}(s)$, obeys the dynamics

$$\partial_t^2 y(s, t) - \partial_s^2 y(s, t) + \eta_{m,d}\partial_t y(s, t) = 0 \qquad [15]$$

with the initial condition $y(s, 0)) \equiv x(s, 0) - x^{\text{eq}}(s)$, $\partial_t y(s, 0) = 0$, and stress-free boundary conditions $\partial_s y(0, t) = \partial_s y(1, t) = 0$. We note that the one remaining parameter

$$\eta_{m,d} \equiv \frac{\tau_m}{\tau_d} = \frac{L\mu}{\sqrt{\alpha}} \qquad [16]$$

is independent of wave speed, which is infinite. The quench limit has an exact Fourier series solution, described in *SI Appendix, Supplementary Methods, section D*.

In Fig. 3 *A* and *B* we compare the solutions of the full nondimensional model (Eq. **8**), the slow wave model (Eq. **10**), and the quench model (Eq. **15**) for two sets of the nondimensional parameters $\eta_{w,d}$ and $\eta_{w,m}$. In these plots, we fix $w = 0.1$ and $g_{\min} = 0$ for simplicity. For $\eta_{w,d} = \eta_{w,m} = 1$ (Fig. 3*A*), the models all behave quite differently because neither limiting case is reached. Decaying oscillations about $l = 0$ are observed for the full and quench model, while the slow wave model does not oscillate because it lacks inertia. The oscillations for the quench and full model have the same frequency (which is proportional to $\eta_{m,d}$, reflecting the resonant frequency of the spring chain) yet different waveforms and amplitudes. For $\eta_{w,d} = 20,\ \eta_{w,m} = 2$ (Fig. 3*B*), the full model and slow wave model are in close agreement.

A stark feature of the full model compared to the quench model is the asymmetry of contraction: In the quench model, all springs instantly have new rest lengths, so all springs relax simultaneously and symmetrically about the center $s = 0.5$. This is not the case for the full model, where the wave first arrives at $s = 0$, causing the springs to begin relaxing before those at $s = 1$. This asymmetry of contraction can be observed in the experimental images of *Spirostomum* and *Vorticella* in Fig. 1 *A* and *B*, and we further illustrate this in Fig. 4 *A*–*C*. In Fig. 4 *D*–*G* we show $x(s, t)$ at several values of t for the full and quench models corresponding to the length trajectories shown in Fig. 3 *A* and *B*.

From the fits to the experimental data of *Vorticella* and *Spirostomum* contracting in water (see *SI Appendix, Supplementary Results, section B*), neither organism is expected to obey the quench-like dynamics, being closer to the slow-wave limit. This implies that the organisms are relaxing appreciably *while* the Ca^{2+} wave traverses their lengths.

D. Scaling Behavior Distinguishes Three Dynamic Regimes. An additional significant difference between the different models is the scaling of the maximum contraction rate with the viscosity. Notably, this has been studied in previous experimental and computational works on *Vorticella* and *Spirostomum*, against which we may validate our model (9, 42, 49).

To explore this scaling behavior, we computed the maximum contraction rate $\dot{\lambda}_{\max} \equiv \max_t|\partial_t\lambda(t)|$ as we varied the nondimensional parameters $\eta_{w,m}$ and $\eta_{w,d}$ in the full, quench, and slow wave models. The results are displayed in Fig. 3 *C* and *D*, again setting $w = 0.1$ and $g_{\min} = 0$ for simplicity. The dynamics of the quench model only depend on the dimensionless parameter $\eta_{m,d}$ (cf. Eq. **15**), and the maximum rate (in units of $L/\tau_m = \sqrt{\alpha}$) asymptotically scales like $\dot{\lambda}_{\max} \sim \eta_{m,d}^{-1} = \eta_{w,m}/\eta_{w,d} = \sqrt{\alpha}/L\mu$. This can be qualitatively understood as follows: as shown in *SI Appendix, Supplementary Methods, section D*, an exact solution for the quench model can be constructed by decomposing the initial condition into spatial Fourier modes and solving for the decay of each mode. Each mode acts like a mass, attached to a wall

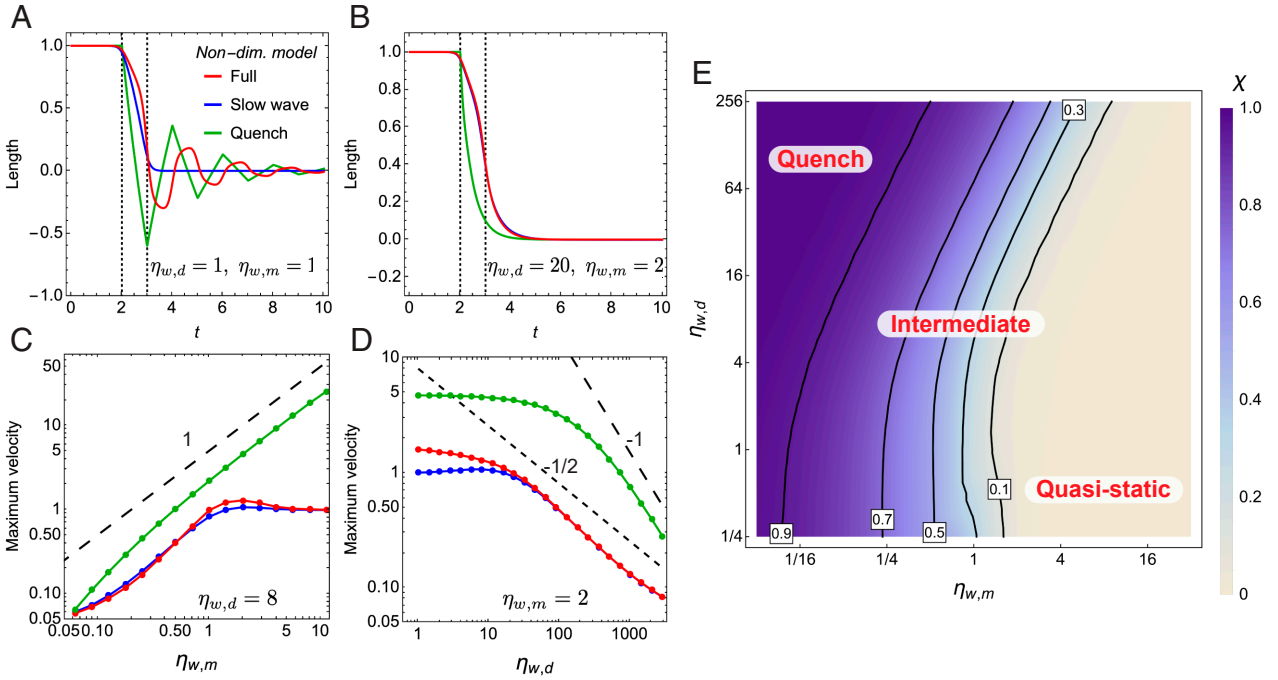

Fig. 3. The nondimensional model and its limiting versions capture key kinematic properties of contraction. (*A*) Nondimensional length $\lambda(t)$ as a function of time for the three versions of the nondimensional model. Parameter values are $\eta_{w,d} = \eta_{w,m} = 1$, $w = 0.1$, $g_{\min} = 0$. The vertical lines at $t = 2$ and 3 indicate the times when the center of the active stretch wave enters and exits the system. The time argument for the quench solution is multiplied by $\eta_{w,m}$ so that it can be compared to the other model solutions. For the quench model, the quench occurs at $t = 2$. (*B*) Same as (*A*) but with $\eta_{w,m} = 2$ and $\eta_{w,d} = 20$. (*C* and *D*) Scaling of $\dot{\lambda}_{\max}$ with $\eta_{w,m}$ (*C*) and $\eta_{w,d}$ (*D*) for the three models. The colors are the same as in (*A*). For panel (*C*), $\eta_{w,d}$ is fixed at 8, while for panel (*D*), $\eta_{w,m}$ is fixed at 2. (*E*) Heatmap of χ, the peak elastic energy stored in the system as a fraction of the maximum possible energy, as $\eta_{w,m}$ and $\eta_{w,d}$ are varied for the full model. Contours are drawn and labeled at selected values of χ.

by a stretched spring with an effective drag constant $\eta_{m,d}$, which is suddenly released (see *SI Appendix*, Eq. **66**). By Stokes' law, the maximum rate should then scale inversely with $\eta_{m,d}$ as observed.

For both the full and slow wave models, $\dot{\lambda}_{\max} \sim \eta_{w,m}$ up to a point at which $\dot{\lambda}_{\max}$ plateaus at 1. This results from the contraction speed not significantly exceeding the speed of the

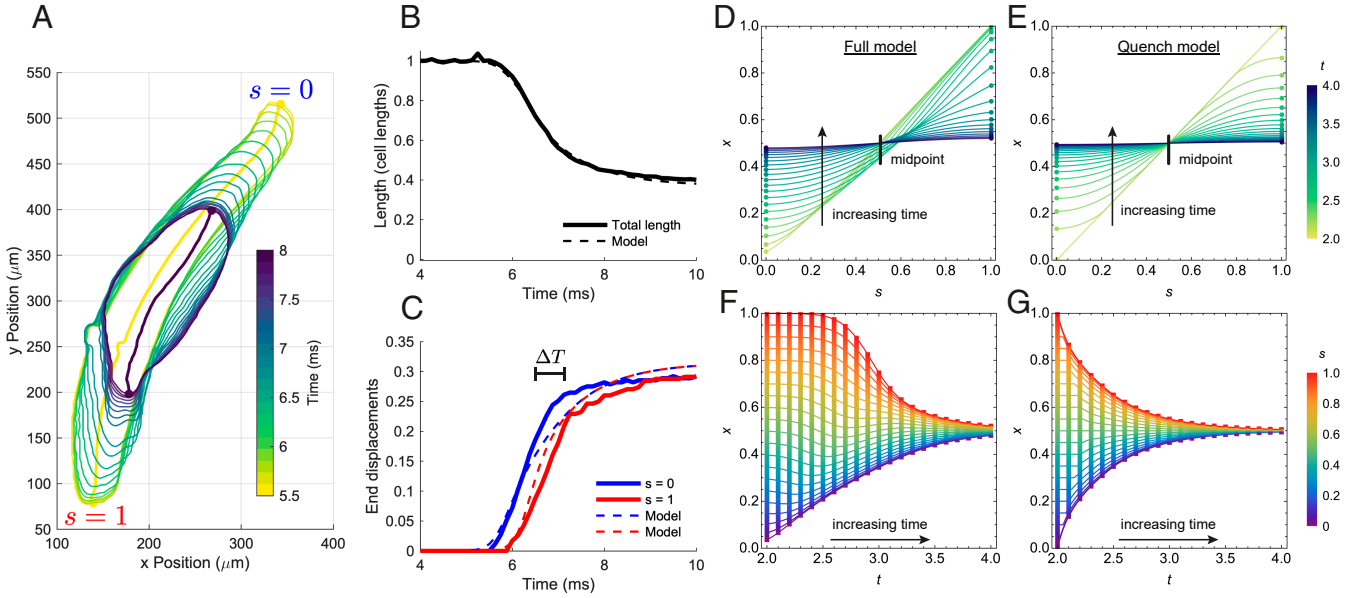

Fig. 4. Asymmetric contraction of *Spirostomum*. (*A*) A sequence of contours of *Spirostomum* obtained from 8,000-Hz video imaging. Colors range from yellow to purple as time ranges from 5.5 ms to 8 ms. The initial and final midlines, whose arc lengths determine the measured length of the organism, are drawn in yellow and purple. (*B*) The trajectory of the length during this contraction event. The dashed curved line shows the trajectory of the simulated model, which was fit to match the experimentally measured solid curve. (*C*) The displacement trajectories of the top (blue) and bottom (red) ends of the midlines and the corresponding quantities in the fitted model are shown as dashed curves. These displacements were measured by projecting the endpoints to the initial midline curve and computing the arc length from the end to the projected point. Asymmetric contraction can be observed as the top end begins contracting before the bottom end (by a time difference labeled ΔT), a feature that the fitted model reproduces. (*D* and *E*) Corresponding to Fig. 3 *A* and *B*, the entire $x(s,t)$ curves for the full and quench models. The colors in these panels range from yellow to blue as t increases from 2 to 4 in steps of 0.1. Panels (*F*) and (*G*) show the same curves as a function of t, rather than s.

traveling active stretch wave, which is defined as 1 in these units. Interestingly, for both models $\dot{\lambda}_{\max}$ (in units of $L/\tau_w = V$) asymptotically scales like $\dot{\lambda}_{\max} \sim \eta_{w,d}^{-1/2}$. To understand this, recall that the slow wave model can be formally mapped to the diffusion equation with a source term (cf. Eqs. **10** and **13**). The dynamics are thus characterized by the "diffusion constant" $\zeta = \eta_{w,m}^2/\eta_{w,d} = \alpha/V\mu L$. For diffusion, it is known that an initial perturbation to the system spreads out over time with a length scale that grows like $\sqrt{\zeta t}$, which implies that the corresponding rate scales like $\dot{\lambda}_{\max} \sim \zeta^{1/2} = \sqrt{\alpha/V\mu L}$. This fact explains both the observed scaling $\dot{\lambda}_{\max} \sim \eta_{w,m}$ up to its saturation at 1, and the asymptotic scaling $\dot{\lambda}_{\max} \sim \eta_{w,d}^{-1/2}$. We emphasize that in Fig. 3, we have assumed the wave width $W = 0.1\ L$ scales with the length L; as demonstrated in *SI Appendix*, Fig. S2, different scaling behaviors result if one varies the uncontracted length L while holding the wave width W fixed. In *SI Appendix*, Fig. S4 we show that this predicted scaling fits our experimental data for *Spirostomum*.

In refs. 42 and 49, the scaling of $\dot{\lambda}_{\max}$ with the solution viscosity ν for *Vorticella* is measured to be $\dot{\lambda}_{\max} \sim \nu^{-1/2}$ (Fig. 5*A*). This is consistent with our observed scaling $\dot{\lambda}_{\max} \sim \zeta^{1/2}$ for the full and slow wave models when holding all other parameters constant and only varying μ (which is proportional to ν). Our model thus exhibits the scaling observed in existing experimental data for *Vorticella*. We note that an alternative description for the $\nu^{-1/2}$ scaling based on power-limited contraction was provided in ref. 42. Our explanation here does not involve a physical argument about power conservation and follows solely from the dynamical equations. It may be possible to show that the energy-based argument is equivalent to the dynamical one presented here, but doing so would likely require a more detailed treatment of thermodynamics of the Ca^{2+} wave (as in ref. 67), and we leave this to future work.

Scaling data for *Spirostomum* are available in refs. 8 and 9 (Fig. 5*B*). In these experiments, to aid imaging, the cells are confined in either a narrow agar channel (blue points) or between a microscope slide and a glass coverslip (orange points). Depending on the confinement method, the scaling appears consistent with either $\dot{\lambda}_{\max} \sim \nu^{-1}$, corresponding to the quench regime, or $\dot{\lambda}_{\max} \sim \nu^{-1/2}$. Our fits in Fig. 2, together with observation of the asymmetric contraction dynamics (Fig. 5*A*), suggest that *Spirostomum* should not be in the quench regime. The quench-like scaling may be an artifact of using pressure on the coverslips to prevent the organisms from swimming out of view; we speculate that this pressure could hinder contraction during the traversal of the wave, effectively quenching the springs. The imaging rate in refs. 8 and 9 (800 Hz) may also be too low to resolve the maximum in the contraction rate profile precisely. We thus performed our own measurements of the contraction of free-swimming *Spirostomum* using a high-speed camera, recording at a minimum of 2,000 Hz. The results, displayed in Fig. 5*C*, are consistent with the predicted scaling $\dot{\lambda}_{\max} \sim \nu^{-1/2}$, though we cannot conclusively exclude the scaling $\dot{\lambda}_{\max} \sim \nu^{-1}$. We note that the low $\dot{\lambda}_{\max}$ at 1 cP is consistent with the predicted roll-off at low viscosity shown in Fig. 3*D*.

The roll-off corresponds to an approach toward a third dynamic regime, which occurs when the active stretch wave is sufficiently slow, or the springs can sufficiently overcome the drag resistance to follow the active stretch wave very closely, with little deviation from equilibrium. In this "quasi-static" limit, there is no dependence of $\dot{\lambda}_{\max}$ on either the stiffness or drag since the contraction speed is solely determined by the speed of the active stretch wave. This regime occurs in the slow wave model when $\zeta \gg 1$, explaining the approach toward $\dot{\lambda}_{\max} = 1$ for large $\eta_{w,m}$ and small $\eta_{w,d}$ in Fig. 3 *C* and *D*. The three scaling regimes—the quench regime ($\dot{\lambda}_{\max} \sim \nu^{-1}$), the intermediate regime ($\dot{\lambda}_{\max} \sim \nu^{-1/2}$), and the quasi-static regime ($\dot{\lambda}_{\max} \sim \nu^{0}$)—fully characterize the qualitative dynamical behavior of myoneme contraction.

To summarize the dynamical behavior of the system as a function of $\eta_{w,d}$ and $\eta_{w,m}$, in *SI Appendix, Supplementary Methods, section E* we introduce the dimensionless quantity χ, which measures the peak elastic energy stored in the system as a fraction of the maximum possible energy which is achieved in

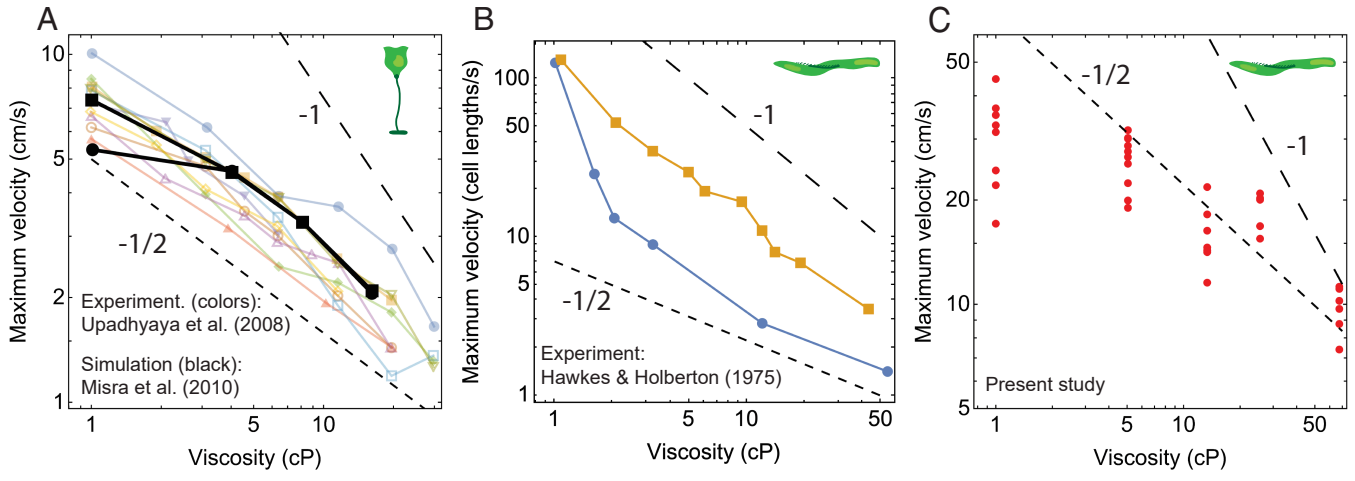

Fig. 5. Experimentally measured contraction rate scaling. (*A*) Published data on the maximum contraction rate of *Vorticella* in solutions of different viscosities. Each colored line represents a single cell exposed to varying viscosities; these data are from figure 3B of ref. 42. The black points represent results from simulations, reproduced from figure 4A in ref. 49. The circle and square represent two values of the elastic stalk's Young's modulus. (*B*) Published data from figure 2 of ref. 9 on the maximum contraction rate of *Spirostomum* in different viscosities and confinement methods: Orange represents a setup using plane parallel glass coverslips, and blue represents a setup using an agar channel. Each point represents an average of 10 to 23 measurements, and connecting lines are drawn to guide the eye. (*C*) Our measurements of the maximum contraction rate of free-swimming *Spirostomum* in solutions of different viscosities. The published data were extracted from refs. 9, 42, and 49 using WebPlotDigitizer (66).

the quench limit. In Fig. 3*E*, we plot χ over $\eta_{w,m} \in [1/32, 32]$ and $\eta_{w,d} \in [1/4, 256]$, and in *SI Appendix*, Fig. S1 we show corresponding trajectories of the energy and length for these conditions. Let us imagine fixing all parameters except the spring stiffness and the viscosity. Fig. 3*E* then illustrates the system's ability to respond to the active stretch wave under different mechanical and environmental conditions: for small $\eta_{w,m}$, corresponding to soft springs, the system stores a large fraction of the possible amount of internal energy ($\chi \approx 1$), but this fraction decreases as the drag, proportional to $\eta_{w,d}$, decreases. By contrast, for large $\eta_{w,m}$, the springs closely follow the active stretch wave and never accumulate much internal energy ($\chi \approx 0$), and the amount that does accumulate decreases as the drag decreases. This energetic perspective thus provides a unified way to understand the dynamic regimes for organisms using Ca^{2+}-based motion.

3. Discussion

A. Summary. We present a minimal mathematical model of myoneme contraction that captures the kinematic features of the organisms *Spirostomum* and *Vorticella*, which exhibit different shapes, sizes, and myoneme arrangements. This model suggests that a fast-traveling wavefront of active stretch, underpinned by rapid Ca^{2+} kinetics, synchronizes contraction across the organism's length. Using an auxiliary reaction–diffusion model for the Ca^{2+} dynamics, we derive scaling relationships for the speed and width of the active stretch wave that enters the mechanical model. These parameters dictate the rate of chemical driving of the myoneme network. Through nondimensionalization, we determine the minimal independent set of parameters controlling contraction and further examine two limiting cases: a quench limit and a slow wave limit. The latter approximately applies to both *Spirostomum* and *Vorticella* in water, as confirmed by fitting the model to experimentally obtained length trajectories. We formally map the dynamics in this limit to the well-studied diffusion equation, with the unitless parameter ζ playing the role of the diffusion constant. The key geometric and mechanical factors that control contractile dynamics include length, stiffness, wave speed, and drag on the organism. These factors manifest through various nondimensional combinations in the different dynamical regimes outlined above. Our analysis reveals three such regimes, each with distinct kinematic signatures such as the symmetry of contraction about the organism's midpoint and the exponent with which the maximum contraction rate scales with viscosity. We further differentiate these regimes by a quantity representing the peak elastic energy stored in the organism relative to the maximal possible value attained in the quench limit.

B. Biological Implications of Dynamic Regimes. It is worthwhile to consider the possible biological implications of the three dynamic regimes. In the quasi-static regime, the myoneme contractile apparatus remains at mechanical equilibrium while the Ca^{2+} wave traverses the organism's length. In this limit, the contractile speed is fully determined by the wave speed V and does not scale with other parameters. The dissipation of chemical energy is minimized at the expense of the speed of motion. The marine protist *Acantharia* reportedly has myoneme-based spicules that are used to regulate buoyancy by contracting in a Ca^{2+}-powered process that is two orders of magnitude slower than contraction in *Spirostomum* or *Vorticella* (19, 29). In this case, contraction may occur quasi-statically. Conversely, the quench regime attains the highest contractile velocities. These high speeds consequently dissipate the most energy because the myoneme apparatus deviates the furthest from mechanical equilibrium. This regime would be suited to processes in which large speeds are physiologically important. For example, *Spirostomum* excites contraction of nearby organisms through "hydrodynamic trigger waves," requiring it to move sufficiently rapidly to disturb the fluid, dissipating energy in the process (10). The intermediate regime, where we place the contraction of *Vorticella* and *Spirostomum*, is expected to achieve a balance between thermodynamic efficiency and biological functionality. While myoneme-based systems are predominantly found in ciliated protists, similar ATP-independent contractile protein networks exist in a wide range of other organisms across taxa, facilitating a diverse set of biological functions (8–10, 15–27). If similar mechanochemical dynamics apply in those organisms, then various selection pressures may favor a particular regime for each function.

C. Comparison to Traditional Latch-Mediated Systems. The theory of latch-mediated spring actuation (LaMSA) provides a general description of motion characterized by a fast unlatching event that releases stored elastic energy (68–70). It has been applied to analyze macroscopic biomechanical processes like the striking of a Mantis shrimp's claw and a human finger snap (71, 72). One may expect that LaMSA also explains myoneme-based contraction, but here energy is stored in the form of a difference in Ca^{2+} chemical potential between the cytosol and the endoplasmic reticulum, and release of a "chemical latch" corresponds to initiation of a traveling wave of Ca^{2+} ions. In addition to this difference in the energy storage medium, LaMSA is designed to apply to macroscopic systems, neglecting the strong dissipative forces which are unavoidable at the cellular level. Furthermore, in myonemes, contraction occurs over an approximately continuous spatial domain of many small elastic elements connected together, compared to the discrete mechanical elements considered in LaMSA. These qualitative features of traditional LaMSA systems compared to the myoneme-based "chemical latch" are illustrated in Fig. 6. Outside the quench limit, the Ca^{2+} wave, which loads mechanical energy into the system, has a finite traversal time. This means that the system can begin relaxing before the energy has been fully loaded. This is another key distinction from traditional LaMSA systems, which are assumed to be fully loaded before relaxing. LaMSA systems also include a constraint force which is lacking in free-swimming organisms like *Spirostomum*. Exploring the implications of adding constraint forces to myoneme-based systems would be an interesting direction for future research. For example, fixing the ends of *Spirostomum* and then releasing them after the Ca^{2+} wave has passed would allow artificially pushing the contraction process into the quench regime. Although how *physical* latches mediate energy flow has only recently been appreciated in biology (69, 73), our model offers a guiding framework for how a *chemical* latch dynamically controls and tunes force output in ultrafast single-cell organisms.

D. Implications for Synthetic Biology. Finally, our model offers valuable insights for engineering myoneme-based synthetic systems. Researchers have recently demonstrated the feasibility of reconstituting myonemes in vitro and exogenously controlling them using light-patterned Ca^{2+} release (74). Myoneme-based systems, therefore, provide a mechanism for exerting mechanical forces at subcellular scales, with orthogonal chemistry to light-controllable actomyosin and kinesin-microtubule systems

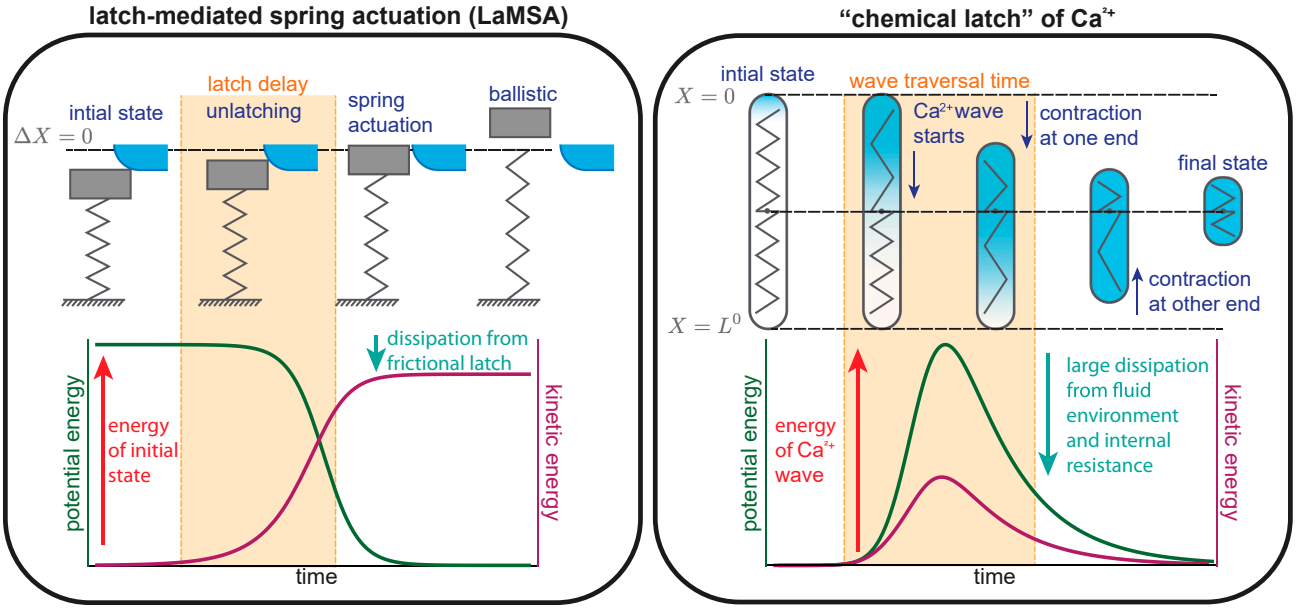

Fig. 6. Schematic illustration of a chemical latch. The *Left* panel, adapted from ref. 68, illustrates a mechanical latch-and-spring system. A latch, shown in blue, slides frictionally off of a compressed spring, shown in gray, which allows for a fast release of the stored potential energy. The finite time during which the latch slides is highlighted in orange. The potential and kinetic energies of the system are schematically plotted at the bottom. At smaller scales, such as the scale of a single-cell organism like *Spirostomum*, a different paradigm accounts for the chemical nature of mechanical activation (via a traveling Ca^{2+} wave). This is illustrated in the *Right* panel, where analogous features of the dynamics in the macroscopic case are shown in the corresponding colors. The traveling wave is shown as a blue gradient, which controls the local rest length (indicated as the number of ridges) of internal springs, shown in gray.

(75–79). Our model uncovers several critical parameters that can modulate the dynamics of myoneme contraction. For example, increasing cross-linking would enhance the effective α, elevating the solution viscosity would raise the effective μ, and increasing the effective light-activated Ca^{2+} release rate or reducing Ca^{2+} buffering (thus increasing D_C) would adjust V and W of the active stretch wave. By controlling these experimental parameters, researchers can explore the various regimes identified in this work, paving the way for designing synthetic cells equipped with myoneme-based artificial cytoskeletons that harness the full potential of ultrafast contraction dynamics.

Materials and Methods

Ca^{2+} Dynamics. The dependence of the active stretch $g(S,T)$ on the local bound Ca^{2+} concentration may be modeled using the instantaneous linear relation (49)

$$g(S,T) = 1 - (1 - g_{\min})\frac{B(S,T)}{B_{\text{tot}}}, \qquad [17]$$

where $B(S,T)$ is the local concentration of Ca^{2+} bound to myoneme fibers and B_{tot} is the total concentration of binding sites (which is assumed to be uniform over the spatial domain). Finding $g(S,T)$ then requires specifying the dynamics for the bound Ca^{2+} profile $B(S,T)$. To avoid introducing extra variables, we first analyze the complete dynamics for $B(S,T)$ by extending a tractable model for a traveling Ca^{2+} wave developed by Kupferman *et al.* (58), and we then use results of this analysis to determine an approximate form for $g(S,T)$ to use in the mechanical model.

The Kupferman model for a traveling Ca^{2+} wave is

$$\partial_T C = D_C \partial_S^2 C - \Gamma C + J\Theta(C - C_0). \qquad [18]$$

Here, $C(S,T)$ is the concentration profile of cytosolic Ca^{2+} which diffuses with a diffusion constant D_C, leaks from the cytosolic compartment with a first-order rate constant Γ, and is released into the cytosol by internal stores at a spatially dependent rate $J\Theta(C-C_0)$. This last term involves a Heaviside function $\Theta(C-C_0)$, which approximates the kinetics of calcium-induced calcium release (63). It "turns on" when the local Ca^{2+} concentration $C(S,T)$ exceeds a spatially uniform threshold C_0, at which point Ca^{2+} is locally released into the cytosol at a rate J. The authors of ref. 58 show that the speed of the traveling wave is given by Eq. **5**.

We extend the Kupferman model to allow cytosolic Ca^{2+} to bind to the myoneme assembly. This introduces the variable $B(S,T)$ for the local concentration of myoneme-bound Ca^{2+}, and the coupled dynamical equations for C and B are

$$\partial_T C = D_C \partial_S^2 C - \Gamma C + J\Theta(C - C_0) - K_+ C(B_{\text{tot}} - B) + K_- B \qquad [19]$$

$$\partial_T B = K_+ C(B_{\text{tot}} - B) - K_- B. \qquad [20]$$

Here, K_+ is the second-order rate constant for binding of cytosolic Ca^{2+} to open myoneme binding sites, which have concentration $B_{\text{tot}} - B$. K_- is the first-order rate constant for the subsequent unbinding of myoneme-bound Ca^{2+}.

In *SI Appendix, Supplementary Methods, section B*, we analyze Eqs. **19** and **20** under mild simplifying assumptions to show that: i) the function $B(S,T)$ is well approximated by a traveling wave with a sigmoidal profile:

$$\frac{B(S,T)}{B_{\text{tot}}} = 1 - \frac{1}{1 + e^{-(S-VT)/W}}, \qquad [21]$$

ii) its speed V is equal to the speed of diffusing Ca^{2+} wave (cf. Eq. **5**), and iii) its width W can be expressed in terms of the chemical parameters according to Eq. **6**.

Combing Eqs. **17** and **21** gives the following form for the nonautonomous active stretch:

$$g(S,T) = g^*(S - VT) = g_{\min} + \frac{1 - g_{\min}}{1 + e^{-(S-V(T-O))/W}}. \qquad [22]$$

The additional parameter O is a time that allows an adjustable offset between $T = 0$ and the time $T = O$ when the center of the wave arrives at $S = 0$. This allows shifting time to achieve acceptable numerical agreement between boundary and initial conditions, as described in *Materials and Methods*, Computational methods.

Experimental Methods. We obtained *Spirostomum* organisms from Carolina Biological and cultured them at room temperature. We prepared culturing medium by mixing one part boiled hay medium solution (Ward's Science, 470177-390), four parts boiled spring water, and two boiled wheat grains (Carolina, Item #132425) as described previously (36). We inoculated organisms into fresh media approximately twice per week. For imaging, we pipetted several organisms at a time into microscopy slides with multiple channels (Ibidi, μ-Slide VI 0.4) or with multiple wells (Ibidi, μ-Slide 8-well). The channels are 400 μm high, allowing the organisms to swim and contract without confinement.

Our *Vorticella* samples were collected from Morse Pond near the Marine Biological Laboratory. We dissected small pieces of plant material to which individual or small groups of *Vorticella* were attached. We added these pieces of plant matter, along with enough imaging medium to cover them, into 8-well coverslip-bottomed sample chambers (Ibidi, μ-Slide 8-well).

To alter the viscosity, we prepared stock solutions of Ficoll PM 400 (Sigma F4375) in water and diluted them to concentrations between 3% and 12% (weight per volume). In the case of *Spirostomum*, we pipetted organisms directly into the Ficoll solution. In the case of *Vorticella*, we rinsed the samples several times with the solution within the sample chamber to ensure that the appropriate viscosity was reached. In both cases, slow pipetting was important to prevent shearing of the organisms in the high-viscosity solutions. To calculate viscosity ν as a function of percentage p of Ficoll in water, we used the calibration function $\nu = e^{0.162p}$ reported in refs. 80 and 81.

We performed brightfield imaging on either a Zeiss inverted microscope equipped with a 0.55 NA condenser, a 0.63× defocusing lens, DIC optics, and a 10× air objective or a Nikon Ti2 equipped with a 2× (MRD70020) or 10× (MRD70170) air objective. In both cases, we collected images using a pco.dimax CS camera equipped with at least 2,000 and up to 10,000 Hz.

For quantifying *Spirostomum* images, we first used Fiji (82) to threshold the images to identify the pixels associated with the organisms, and then we used Matlab to run Morphometrics (83) to obtain the cell contours. We used the pill-mesh option of Morphometrics to obtain cell shape and length. See *SI Appendix*, Fig. S3 and Movie S3 for a visualization of this mesh generation procedure.

For quantifying *Vorticella* length over time, we manually tracked the position of the end of the stalk attached to the cell body using home-built Python software.

Computational Methods. All numerical integration was performed with Mathematica's NDSolve function, using the method of lines option with a spatial discretization based on tensor product grids. The accuracy and precision goals were set high enough to ensure reasonable numerical convergence. To achieve agreement between the initial conditions Eq. **4** and the boundary conditions Eq. **3**, we increased the parameter O in Eq. **22** so that $g(S, 0) \approx 1$ across the computational domain. To solve the quench model Eq. **15**, we evaluate the exact solution given in *SI Appendix*, Eq. **60** using 50 terms in the Fourier expansion.

Data, Materials, and Software Availability. All study data are included in the article and/or supporting information. Code and data used for the results in this paper can be found at https://github.com/bhamla-lab/myonememodelPNAS2023 (84).

ACKNOWLEDGMENTS. We wish to thank Shane Terrell for help setting up the experiments, Vincent Boudreau for providing samples of *Vorticella* in fresh pond water, Joe Brzostowski, Tanner Fadero, and Sam Lord for technical assistance with the microscopy, KC Huang and Tristan Ursell for providing the Morphometrics software, and Joe Lannan, Christian Pagán-Medina, Joël Lemière, and Jane Maienschein for helpful discussions. This work was mainly supported by NSF awards EF-1935260, EF-1935261, and EF-1935262. S.V. was supported by the National Institute of General Medical Sciences of the NIH under Award No. R35GM147400. The content is solely the responsibility of the authors and does not necessarily represent the official views of the NIH. C.F. acknowledges support from the University of Chicago through a Chicago Center for Theoretical Chemistry Fellowship. M.S.B. acknowledges funding support from NIH Grant R35GM142588; NSF Grant MCB-1817334; NSF CAREER IOS-1941933; and a gift from the Open Philanthropy Project. F.C. acknowledges funding support from NIH Grant R35GM141796. We acknowledge the University of Chicago's Research Computing Center for computing resources, the Marine Biological Laboratory Whitman Summer Investigator Program and the Physiology Course for the use of microscopy equipment, and Zeiss and pco. for loans of cameras.

Author affiliations: [a]Department of Chemistry and James Franck Institute, University of Chicago, Chicago, IL 60637; [b]Department of Cell and Tissue Biology, University of California, San Francisco, CA 94143; [c]School of Chemical and Biomolecular Engineering, Georgia Institute of Technology, Atlanta, GA 30318; [d]Department of Biology, Drake University, Des Moines, IA 50311; and [e]Department of Physics, North Carolina State University, Raleigh, NC 27607

Author contributions: C.F., A.T.M., X.L., J.E.H., F.C., M.W.E., S.V., A.R.D., and M.S.B. designed research; C.F., A.T.M., M.W.E., S.V., A.R.D., and M.S.B. performed research; C.F., A.T.M., M.W.E., S.V., A.R.D., and M.S.B. analyzed data; and C.F., A.T.M., M.W.E., S.V., A.R.D., and M.S.B. wrote the paper.

The authors declare no competing interest.

1. M. Murrell, P. W. Oakes, M. Lenz, M. L. Gardel, Forcing cells into shape: The mechanics of actomyosin contractility. *Nat. Rev. Mol. Cell Biol.* **16**, 486–498 (2015).
2. W. F. Marshall, Don't blink: Observing the ultra-fast contraction of spasmonemes. *Biophys. J.* **94**, 4–5 (2008).
3. T. Weis-Fogh, W. Amos, Evidence for a new mechanism of cell motility. *Nature* **236**, 301–304 (1972).
4. J. Cachon, M. Cachon, Movement by non-actin filament mechanisms. *Biosystems* **14**, 313–326 (1981).
5. D. H. Lynn, *The Ciliated Protozoa: Characterization, Classification, and Guide to the Literature* (Springer, 2008).
6. W. Amos, Reversible mechanochemical cycle in the contraction of *Vorticella*. *Nature* **229**, 127–128 (1971).
7. S. Ryu, R. E. Pepper, M. Nagai, D. C. France, *Vorticella*: A protozoan for bio-inspired engineering. *Micromachines* **8**, 4 (2016).
8. R. Hawkes, D. Holberton, Myonemal contraction of *Spirostomum*. I. Kinetics of contraction and relaxation. *J. Cell. Physiol.* **84**, 225–235 (1974).
9. R. Hawkes, D. Holberton, Myonemal contraction of *Spirostomum*. II. Some mechanical properties of the contractile apparatus. *J. Cell. Physiol.* **85**, 595–602 (1975).
10. A. J. Mathijssen, J. Culver, M. S. Bhamla, M. Prakash, Collective intercellular communication through ultra-fast hydrodynamic trigger waves. *Nature* **571**, 560–564 (2019).
11. J. Zhang *et al.*, Giant proteins in a giant cell: Molecular basis of ultrafast Ca^{2+}-dependent cell contraction. *Sci. Adv.* **9**, eadd6550 (2023).
12. M. M. Slabodnick, W. F. Marshall, Stentor coeruleus. *Curr. Biol.* **24**, R783–R784 (2014).
13. E. Newman, Contraction in *Stentor coeruleus*: A cinematic analysis. *Science* **177**, 447–449 (1972).
14. S. M. Coyle *et al.*, Coupled active systems encode an emergent hunting behavior in the unicellular predator Lacrymaria olor. *Curr. Biol.* **29**, 3838–3850 (2019).
15. Y. Moriyama, H. Okamoto, H. Asai, Rubber-like elasticity and volume changes in the isolated spasmoneme of giant *Zoothamnium* sp. under Ca^{2+}-induced contraction *Biophys. J.* **76**, 993–1000 (1999).
16. R. Moreton, W. Amos, Electrical recording from the contractile ciliate *Zoothamnium geniculatum ayrton*. *J. Exp. Biol.* **83**, 159–167 (1979).
17. M. Melkonian, P. L. Beech, C. Katsaros, D. Schulze, "Centrin-mediated cell motility in algae" in *Algal Cell Motility* (Springer, 1992), pp. 179–221.
18. M. Ishida, Y. Shigenaka, K. Taneda, Studies on the mechanism of cell elongation in *Blepharisma japonicum*. I. A physiological mechanism how light stimulation evokes cell elongation. *Eur. J. Protistol.* **25**, 182–186 (1989).
19. J. Febvre, The myoneme of the Acantharia (Protozoa): A new model of cellular motility. *Biosystems* **14**, 327–336 (1981).
20. M. Ando, Y. Shigenaka, Structure and function of the cytoskeleton in heliozoa: I. Mechanism of rapid axopodial contraction in *Echinosphaerium*. *Cell Motil. Cytoskelet.* **14**, 288–301 (1989).
21. B. Viguès, R. Damaj, The adhesive disc in the mobilid ciliate *Trichodina pediculus*: Evidence for centrin-related, calcium-sensitive filaments. *Cytoskeleton* **69**, 113–124 (2012).
22. M. Kawachi, I. Inouye, Ca^{2+}-mediated induction of the coiling of the haptonema in *Chrysochromulina hirta* (Prymnesiophyta = Haptophyta) *Phycologia* **33**, 53–57 (1994).
23. G. McFadden, D. Schulze, B. Surek, J. L. Salisbury, M. Melkonian, Basal body reorientation mediated by a Ca^{2+}-modulated contractile protein *J. Cell Biol.* **105**, 903–912 (1987).
24. J. Cachon, M. Cachon, An unusual mechanism of cell contraction: Leptodiscinae dinoflagellates. *Cell Motil.* **4**, 41–55 (1984).
25. M. Knoblauch *et al.*, ATP-independent contractile proteins from plants. *Nat. Mater.* **2**, 600–603 (2003).
26. M. Knoblauch, W. S. Peters, Forisomes, a novel type of Ca^{2+}-dependent contractile protein motor *Cell Motil. Cytoskelet.* **58**, 137–142 (2004).
27. W. T. Huck, Responsive polymers for nanoscale actuation. *Mater. Today* **11**, 24–32 (2008).
28. H. Hoffmann-Berling, The mechanism of a new contraction cycle distinct from muscle contraction. *Biochim. Biophys. Acta* **27**, 247–255 (1958).
29. J. Febvre, C. Febvre-Chevalier, Motility processes in Acantharia (Protozoa). III. Calcium regulation of the contraction–relaxation cycles of in vivo myonemes. *Biol. Cell* **67**, 251–261 (1989).
30. K. Katoh, Y. Naitoh, Control of cellular contraction by calcium in *Vorticella*. *J. Exp. Biol.* **189**, 163–177 (1994).
31. Y. Yokoyama, H. Asai, Contractility of the spasmoneme in glycerinated *Vorticella* stalk induced by various divalent metal and lanthanide ions. *Cell Motil. Cytoskelet.* **7**, 39–45 (1987).
32. W. Amos, Structure and coiling of the stalk in the peritrich ciliates *Vorticella* and *Carchesium*. *J. Cell Sci.* **10**, 95–122 (1972).

33. L. Routledge, W. Amos, B. Gupta, T. Hall, T. Weis-Fogh, Microprobe measurements of calcium binding in the contractile spasmoneme of a vorticellid. *J. Cell Sci.* **19**, 195–201 (1975).
34. A. R. Jones, T. L. Jahn, J. R. Fonseca, Contraction of protoplasm. I. Cinematographic analysis of the anodally stimulated contraction of *Spirostomum ambiguum*. *J. Cell. Physiol.* **68**, 127–133 (1966).
35. T. Ochiai, H. Asai, K. Fukui, Hysteresis of contraction-extension cycle of glycerinated *Vorticella*. *J. Protozool.* **26**, 420–425 (1979).
36. L. Xu , M. Bhamla , Biophysical mechanism of ultrafast helical twisting contraction in the giant unicellular ciliate *Spirostomum ambiguum*. bioRxiv [Preprint] (2019). https://doi.org/10.1101/854836 (Accessed 23 July 2021).
37. Y. Moriyama, S. Hiyama, H. Asai, High-speed video cinematographic demonstration of stalk and zooid contraction of *Vorticella convallaria*. *Biophys. J.* **74**, 487–491 (1998).
38. S. Ryu, P. Matsudaira, Unsteady motion, finite Reynolds numbers, and wall effect on *Vorticella convallaria* contribute contraction force greater than the stokes drag. *Biophys. J.* **98**, 2574–2581 (2010).
39. S. Ryu, M. J. Lang, P. Matsudaira, Maximal force characteristics of the Ca^{2+}-powered actuator of *Vorticella convallaria Biophys. J.* **103**, 860–867 (2012).
40. J. Zhou, S. Ryu, D. Admiraal, Flow and transport effect caused by the stalk contraction cycle of *Vorticella convallaria*. *Biomicrofluidics* **11**, 034119 (2017).
41. E. G. Chung, S. Ryu, Stalk-length-dependence of the contractility of *Vorticella convallaria*. *Phys. Biol.* **14**, 066002 (2017).
42. A. Upadhyaya *et al*., Power-limited contraction dynamics of *Vorticella convallaria*: An ultrafast biological spring. *Biophys. J.* **94**, 265–272 (2008).
43. M. C. Marchetti *et al*., Hydrodynamics of soft active matter. *Rev. Mod. Phys.* **85**, 1143 (2013).
44. G. Danuser, J. Allard, A. Mogilner, Mathematical modeling of eukaryotic cell migration: Insights beyond experiments. *Annu. Rev. Cell Dev. Biol.* **29**, 501 (2013).
45. J. Prost, F. Jülicher, J. F. Joanny, Active gel physics. *Nat. Phys.* **11**, 111–117 (2015).
46. K. Popov, J. Komianos, G. A. Papoian, MEDYAN: Mechanochemical simulations of contraction and polarity alignment in actomyosin networks. *PLoS Comput. Biol.* **12**, e1004877 (2016).
47. S. L. Freedman, S. Banerjee, G. M. Hocky, A. R. Dinner, A versatile framework for simulating the dynamic mechanical structure of cytoskeletal networks. *Biophys. J.* **113**, 448–460 (2017).
48. F. Nédélec, T. Surrey, A. C. Maggs, S. Leibler, Self-organization of microtubules and motors. *Nature* **389**, 305–308 (1997).
49. G. Misra, R. B. Dickinson, A. J. Ladd, Mechanics of *Vorticella* contraction. *Biophys. J.* **98**, 2923–2932 (2010).
50. K. Katoh, M. Kikuyama, An all-or-nothing rise in cytosolic. *J. Exp. Biol.* **200**, 35–40 (1997).
51. H. Shiono, Y. Naitoh, Cellular contraction precedes membrane depolarization in *Vorticella convallaria*. *J. Exp. Biol.* **200**, 2249–2261 (1997).
52. I. Delvendahl *et al*., Reduced endogenous Ca^{2+} buffering speeds active zone Ca^{2+} signaling. *Proc. Natl. Acad. Sci. U.S.A.* **112**, E3075–E3084 (2015).
53. L. Mahadevan, P. Matsudaira, Motility powered by supramolecular springs and ratchets. *Science* **288**, 95–99 (2000).
54. F. Horkay, Polyelectrolyte gels: A unique class of soft materials. *Gels* **7**, 102 (2021).
55. A. Mogilner, G. Oster, Polymer motors: Pushing out the front and pulling up the back. *Curr. Biol.* **13**, R721–R733 (2003).
56. W. S. Slaughter, *The Linearized Theory of Elasticity* (Springer Science & Business Media, 2012).
57. L. E. Kinsler, A. R. Frey, A. B. Coppens, J. V. Sanders, *Fundamentals of Acoustics* (John Wiley & Sons, 2000).
58. R. Kupferman, P. P. Mitra, P. Hohenberg, S. Wang, Analytical calculation of intracellular calcium wave characteristics. *Biophys. J.* **72**, 2430–2444 (1997).
59. J. Gore *et al*., DNA overwinds when stretched. *Nature* **442**, 836–839 (2006).
60. C. Floyd, H. Ni, R. S. Gunaratne, R. Erban, G. A. Papoian, On stretching, bending, shearing, and twisting of actin filaments. I: Variational models. *J. Chem. Theory Comput.* **18**, 4865–4878 (2022).
61. E. Moeendarbary *et al*., The cytoplasm of living cells behaves as a poroelastic material. *Nat. Mater.* **12**, 253–261 (2013).
62. S. Schuster, M. Marhl, T. Höfer, Modelling of simple and complex calcium oscillations: From single-cell responses to intercellular signalling. *Eur. J. Biochem.* **269**, 1333–1355 (2002).
63. G. Dupont, M. Falcke, V. Kirk, J. Sneyd, *Models of Calcium Signalling* (Springer, 2016).
64. H. Ishida, T. Suzaki, Y. Shigenaka, Effect of Mg^{2+} on Ca^{2+}-dependent contraction of a Spirostomum cell model. *Eur. J. Protistol.* **32**, 316–319 (1996).
65. E. M. Ettienne, Control of contractility in Spirostomum by dissociated calcium ions. *J. General Physiol.* **56**, 168–179 (1970).
66. A. Rohatgi, Webplotdigitizer (Version 4.6, Pacifica, California, USA, 2017). https://automeris.io/WebPlotDigitizer (Accessed 25 July 2022).
67. F. Avanzini, G. Falasco, M. Esposito, Thermodynamics of chemical waves. *J. Chem. Phys.* **151**, 234103 (2019).
68. S. Divi *et al*., Latch-based control of energy output in spring actuated systems. *J. R. Soc. Interface* **17**, 20200070 (2020).
69. M. Ilton *et al*., The principles of cascading power limits in small, fast biological and engineered systems. *Science* **360**, eaao1082 (2018).
70. S. J. Longo *et al*., Beyond power amplification: Latch-mediated spring actuation is an emerging framework for the study of diverse elastic systems. *J. Exp. Biol.* **222**, jeb197889 (2019).
71. E. Steinhardt *et al*., A physical model of mantis shrimp for exploring the dynamics of ultrafast systems. *Proc. Natl. Acad. Sci. U.S.A.* **118**, e2026833118 (2021).
72. R. Acharya, E. J. Challita, M. Ilton, M. Saad Bhamla, The ultrafast snap of a finger is mediated by skin friction. *J. R. Soc. Interface* **18**, 20210672 (2021).
73. N. P. Hyun *et al*., Spring and latch dynamics can act as control pathways in ultrafast systems. *Bioinspir. Biomim.* **18**, 026002 (2022).
74. X. Lei, T. Chakrabortty, J. Honts, S. Bhamla, In vitro light-controlled patterns and force generation for synthetic cytoskeletal networks. *Bull. Am. Phys. Soc.* **2022**, B07–003 (2022).
75. M. Nakamura *et al*., Remote control of myosin and kinesin motors using light-activated gearshifting. *Nat. Nanotechnol.* **9**, 693–697 (2014).
76. P. V. Ruijgrok *et al*., Optical control of fast and processive engineered myosins in vitro and in living cells. *Nat. Chem. Biol.* **17**, 540–548 (2021).
77. R. Zhang *et al*., Spatiotemporal control of liquid crystal structure and dynamics through activity patterning. *Nat. Mater.* **20**, 875–882 (2021).
78. T. D. Ross *et al*., Controlling organization and forces in active matter through optically defined boundaries. *Nature* **572**, 224–229 (2019).
79. M. Malik-Garbi *et al*., Scaling behaviour in steady-state contracting actomyosin networks. *Nat. Phys.* **15**, 509–516 (2019).
80. C. J. Lo, "Sodium energetics of chimeric flagellar motors in *Escherichia coli*" PhD thesis, University of Oxford, UK (2007).
81. X. Chen, H. C. Berg, Torque–speed relationship of the flagellar rotary motor of *Escherichia coli*. *Biophys. J.* **78**, 1036–1041 (2000).
82. J. Schindelin *et al*., Fiji: An open-source platform for biological-image analysis. *Nat. Methods* **9**, 676–682 (2012).
83. T. Ursell *et al*., Rapid, precise quantification of bacterial cellular dimensions across a genomic-scale knockout library. *BMC Biol.* **15**, 1–15 (2017).
84. C. Floyd *et al*., Bhamla-lab/myonememodelPNAS2023. GitHub. https://github.com/bhamla-lab/myonememodelPNAS2023. Deposited 18 May 2023.